3. Y. Huang *et al.*, *Science* **294**, 1313 (2001).
4. A. M. Morales, C. M. Lieber, *Science* **279**, 208 (1998).
5. L. Manna, E. C. Scher, A. P. Alivisatos, *J. Am. Chem. Soc.* **122**, 12700 (2000).
6. Y. Xia *et al.*, *Adv. Mater.* **15**, 353 (2003).
7. J. N. Cha, G. D. Stucky, D. E. Morse, T. J. Deming, *Nature* **403**, 289 (2000).
8. J. D. Hartgerink, E. Beniash, S. I. Stupp, *Science* **294**, 1684 (2001).
9. T. Douglas, M. Young, *Nature* **393**, 152 (1998).
10. E. Dujardin *et al.*, *Nano Lett.* **3**, 413 (2003).
11. S.-W. Lee, C. Mao, C. E. Flynn, A. M. Belcher, *Science* **296**, 892 (2002).
12. M. Reches, E. Gazit, *Science* **300**, 625 (2003).
13. S. R. Whaley, D. S. English, E. L. Hu, P. F. Barbara, A. M. Belcher, *Nature* **405**, 665 (2000).
14. C. Mao *et al.*, *Proc. Natl. Acad. Sci. U.S.A.* **100**, 6946 (2003).
15. J. F. Banfield, S. A. Welch, H. Zhang, T. T. Ebert, R. L. Penn, *Science* **289**, 751 (2000).
16. A. P. Alivisatos, *Science* **289**, 736 (2000).
17. C. Flynn, *et al.*, *J. Mater. Chem.* **13**, 2414 (2003).
18. B. D. Reiss *et al.*, in preparation.
19. Single-letter abbreviations for the amino acid residues are as follows: A, Ala; C, Cys; D, Asp; E, Glu; F, Phe; G, Gly; H, His; I, Ile; K, Lys; L, Leu; M, Met; N, Asn; P, Pro; Q, Gln; R, Arg; S, Ser; T, Thr; V, Val; W, Trp; and Y, Tyr.
20. C. F. Barbas III *et al.*, *Phage Display, A Laboratory Manual* (Cold Spring Harbor Laboratory Press, Cold Spring Harbor, NY, 2001).
21. C. Gao *et al.*, *Proc. Natl. Acad. Sci. U.S.A.* **96**, 6025 (1999).
22. P. Malik, R. N. Perham, *Nucleic Acids Res.* **25**, 915 (1997).
23. K. Nam *et al.*, *Nano Lett.*, in press; published online 16 December 2003 (10.1021/nl0347536).
24. W. D. Luedtke, U. Landman, *J. Phys. Chem.* **100**, 13323 (1996).
25. Annealing of the ZnS mineralized viruses for 3 hours on aminosilinized SiO_2 wafers at 400° to 500°C, depending on particle size distribution, was followed by sonication in 1:1 water and ethanol. The suspension of annealed wires was drop coated onto TEM grids for visualization. Increasing the wetability of the substrates was necessary for the alignment of the virus assemblies.
26. Thermal gravimetric analysis was performed on the Perkin Elmer 200 thermogravimetric/differential thermal analysis, with flow gases consisting of air, argon, and forming gas (5% H_2). Samples were prepared by centrifugation of the virus-particle suspension into 1-mg pellets and allowed to dry.
27. TEM samples were analyzed with the JEOL 2010 and 2010–Field Emission Gun (FEG) microscopes. HAADF analysis of the ZnS and CdS samples was performed on the JEOL 2010-FEG. Gantan Digital Micrograph is used to subtract the background of the HRTEM lattice images. Thermal analysis of the CoPt system was performed in situ on the JEOL 200CX microscope operated at 200 kV, with a Gatan heat stage.
28. S. B. Qadri *et al.*, *Phys. Rev. B* **60**, 9191 (1999).
29. X. Duan, C. M. Lieber, *Adv. Mater.* **12**, 298 (2000).
30. C. Ye, G. Meng, Y. Wang, Z. Jiang, L. Zhang, *J. Phys. Chem. B* **106**, 10338 (2002).
31. R. L. Penn, J. F. Banfield, *Geochim. Cosmochim. Acta* **63**, 1549 (1999).
32. S. Sun, C. B. Murray, D. Weller, L. Folks, A. Moser, *Science* **287**, 1989 (2000).
33. Y. H. Huang, H. Okumura, G. C. Hadjipanayis, D. Weller, *J. Appl. Phys.* **91**, 6869 (2002).
34. CoPt wires were synthesized by the interaction of 1 ml of CoPt-specific viruses (10^{12} phage/ml) with 0.5 mM $CoCl_2$ and 0.5 mM H_2PtCl_6 in a 1:1 ratio. In the case of FePt, 1 ml of phage (10^{12} phage/ml) was mixed with 0.01 mM $FeCl_2$ and 0.01 mM H_2PtCl_6. These mixtures were vortexed for 10 min to ensure mixing, and 0.1 M $NaBH_4$ was added to reduce the metals forming the desired nanoparticles. The CoPt and FePt systems were applied directly to SiO TEM grids and annealed under forming gas (5% H_2) to prevent the onset of oxidation for 3 hours at 350°C.
35. K. Barmak *et al.*, *Appl. Phys. Lett.* **80**, 4268 (2002).
36. The virus assembly was reconstructed from the gP8 protein structure obtained from the Protein Data Bank (PDB) (number 1ifj) by application of the appropriate translation vectors. A random number generator was used to realistically incorporate peptide inserts in the gP8 assembly at a given incorporation percentage. The peptide inserts were modeled in the capsid environment with Monte Carlo software MCPRO (*39*) with solvent effects accounted for by the Poisson-Boltzmann toolkit ZAP (*40*).
37. H. Zhu, R. S. Averback, *Philos. Mag. Lett.* **73**, 27 (1996).
38. M. Yeadon, M. Ghaly, J. C. Yang, R. S. Averback, J. M. Gibson, *Appl. Phys. Lett.* **73**, 3208 (1998).
39. MCPRO, Version 1.68; W. L. Jorgensen, Yale University.
40. OpenEye Scientific Software, Cambridge, MA.

41. We thank C. Flynn for valuable discussion. We acknowledge the use of core microscope facilities in the Texas Materials Institute at UT and the Center for Materials Science and Engineering at MIT. Supported by NSF through the Nanotechnology and Interdisciplinary Research Initiative, the Army Research Office, and the Air Force Scientific Research Office.

20 October 2003; accepted 26 November 2003

Boron Nitride Nanomesh

Martina Corso, Willi Auwärter, Matthias Muntwiler, Anna Tamai, Thomas Greber, Jürg Osterwalder*

A highly regular mesh of hexagonal boron nitride with a 3-nanometer periodicity and a 2-nanometer hole size was formed by self-assembly on a Rh(111) single crystalline surface. Two layers of mesh cover the surface uniformly after high-temperature exposure of the clean rhodium surface to borazine $(HBNH)_3$. The two layers are offset in such a way as to expose a minimum metal surface area. Hole formation is likely driven by the lattice mismatch of the film and the rhodium substrate. This regular nanostructure is thermally very stable and can serve as a template to organize molecules, as is exemplified by the decoration of the mesh by C_{60} molecules.

Pairs of boron and nitrogen atoms are isoelectronic to pairs of carbon atoms. Thus, boron nitrides show a structural variety similar to that of carbon solids, including graphitic hexagonal boron nitride (*h*-BN) and diamond-like cubic boron nitride (*c*-BN) (*1*), onion-like fullerenes (*2*), and multi- and single-wall nanotubes (*3*, *4*). Some carbon allotropes, such as C_{60}, are difficult to form as BN analogs, because the formation of B-B or N-N bonds is disfavored, and this property excludes pentagon formation. We report on a form of BN solid that so far has no analog in carbon allotropes. A highly regular metal-supported BN mesh of nanometer dimensions can be grown by high-temperature chemical vapor deposition on Rh(111). The hexagonal mesh has its basis in the planar, *h*-BN–type bonding and consists of two atomic layers.

Weakly physisorbed layers of *h*-BN on metal surfaces have been studied for about a decade (*5*). Well-ordered films can be grown by thermal decomposition of borazine $(HBNH)_3$ on transition metal surfaces (*6*). In all cases studied so far, the film growth was self-limiting at one monolayer (ML); beyond that, the sticking coefficient of the precursor molecule becomes exceedingly small. Most of the work has been concentrated on the lattice-matched system of *h*-BN on Ni(111), where large terraces of one-ML *h*-BN are formed (*7*). The films are insulating in the sense that the B and N electronic states do not contribute to the Fermi sea of the Ni surface (*8*, *9*). Within this ML, the structure is the expected graphitic sheet, yet with a weak corrugation. The N atoms are located on top of the outermost Ni atoms, and the B atoms occupy face-centered cubic adsorption sites of the Ni(111) surface (*10*, *11*). Depending on the preparation conditions, a second coexisting structure can be found in which the B atoms are placed in hexagonal close-packed adsorption sites. Wherever domains of these different structures coalesce, straight defect lines are observed in scanning tunneling microscopy (STM) images (*12*). Although all these studies illustrated the model character of this weakly physisorbed metal-insulator interface, they did not raise expectations for these systems to exhibit self-organization into complex structures on a nano- to mesoscopic-length scale. Here, it is shown that such self-organization within the *h*-BN layer takes place when deposited on Rh(111), where the lattice mismatch of 6.7% produces a high tensile stress.

The preparation procedure consists of exposing the atomically clean Rh(111) surface, which is kept at a temperature of 1070

Physik-Institut, Universität Zürich, Winterthurerstrasse 190, CH-8057 Zürich, Switzerland.

*To whom correspondence should be addressed. E-mail: osterwal@physik.unizh.ch

K, to a borazine vapor pressure of 3×10^{-7} mbar inside an ultrahigh vacuum chamber. After exposure to 40 L (1 Langmuir = 10^{-6} torr s) and consecutive cooling down to room temperature, the regular mesh structure as shown in Fig. 1A was observed in STM images. The B and N coverages on the Rh(111) surface were quantified in situ by means of x-ray photoelectron spectroscopy. Borazine doses between 40 and 360 L, which produced a complete nanomesh film, led to absolute coverages of between 1.5 and 1.75 MLs; i.e., there are about 1.5 BN units per surface Rh atom in the nanomesh. Within the error limits, the films are stoichiometric.

The high degree of periodicity seen in the STM image is found throughout the macroscopic sample area and was confirmed by the low-energy electron diffraction (LEED) pattern (Fig. 2). These data provide a first clue for the atomic structure within the nanomesh. The inplane lattice constant of the hexagonal Rh(111) surface is 2.69 Å. From the principal spots of the nanomesh LEED pattern (Fig. 2B), a hexagonal atomic lattice is deduced also for the BN layer, with a lattice constant of 2.48 ± 0.05 Å. Unlike on Ni(111), where the slightly compressive stress leads to a pseudomorphic film with a weak corrugation, the lattice mismatch on Rh(111) is too large, and the weakly physisorbed *h*-BN layer appears to form with its native lattice constant of 2.50 Å. The superlattice spots around the principal spots indicate a periodicity of 32 ± 1 Å, which corresponds to a supercell of 12-by-12 Rh unit cells, or 13-by-13 *h*-BN unit cells. The LEED data would thus be consistent with the formation of a coincidence lattice or Moiré pattern, but the STM image (Fig. 1A) suggests that only a portion of the superlattice unit cell is occupied by BN cells.

The STM image of Fig. 1B shows a small area of perfect nanomesh and provides some further hints on the detailed structure of its unit cell. Inside each supercell, four distinct gray-scale levels occur (see also the line scan in Fig. 1C). This image was taken with a constant current of 1 nA such that the average tip-to-sample distance was relatively large. The sample bias was –2 eV, and electrons tunneled from occupied states into the tip. In a topographic interpretation, we can identify the darkest level with regions of uncovered Rh surface and the next brighter level with a first *h*-BN layer. The brightest two levels correspond to a second *h*-BN layer, which appears to be pushed out in the regions where the two layers overlap and pulled in toward the Rh surface in the hole regions of the first layer. Combined with the information from the LEED pattern, the following picture emerges (Fig. 3A): The hexagonal nanomesh consists of two atomic mesh layers with open apertures of 2.4 ± 0.2 nm in diameter in the outer layer and probably slightly smaller ones in the inner layer. Mesh wires of 0.9 ± 0.2 nm width are formed by the atomic *h*-BN lattice. The periodicity of the mesh is 3.2 ± 0.2 nm, and the meshes of the two individual layers are offset such as to cover most of the underlying metal surface. The first *h*-BN layer lies essentially flat on the Rh(111), whereas the second one appears like a corrugated sheet that follows the topography of the first. The mechanism underlying this self-assembly is unclear, but symmetry and lattice mismatch likely play a role. Experiments with lower borazine exposures, leading to partial coverages of nanomesh, indicate that self-organization is a concerted process that involves both layers at the same time. Regions of 1-ML *h*-BN do not show ordered structures, and only in condensed second-layer regions does the nanomesh appear (fig. S1).

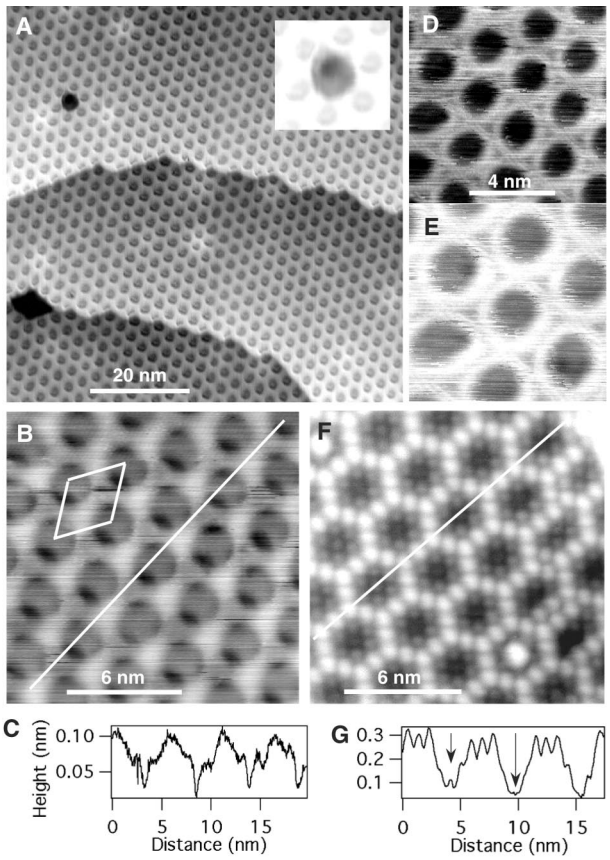

Fig. 1. Constant-current STM images of the boron nitride nanomesh formed by high-temperature decomposition of borazine on a Rh(111) surface. The exposure is 40 L in all cases. (**A**) Large-area survey image taken with a bias voltage of $V_b = -1.0$ V and a tunneling current of $I_t = 2.5$ nA. Two steps on the Rh(111) surface cross the image. The black features are defects in the mesh, one of which is shown with different contrast in the inset. Brighter spots may be related to Ar bubbles in the near-surface region of the substrate (*13*). (**B**) High-resolution image (–2.0 V and 1.0 nA) clearly showing the presence of two layers of mesh that are offset such as to cover most of the Rh(111) surface. The mesh unit cell is indicated. (**C**) Cross-sectional profile along the diagonal white line in (B), indicating the presence of four different height levels within the individual unit cells. (**D**) High-resolution image taken with tunneling conditions (–2.0 V and 3.5 nA) that bring the tip closer to the surface. (**E**) Same as in (D) but with –2.0 V and 4.5 nA, showing contrast in the bottom mesh layer. (**F**) High-resolution image of a region of *h*-BN nanomesh decorated by C_{60} molecules (–2.0 V and 1.5 nA). Individual molecules are imaged throughout this region, following closely the topography of the mesh. The positions in the hole centers are occupied by either zero or one C_{60} molecule; at two places, large protrusions may represent additional corralled molecules. (**G**) Cross-sectional profile along the diagonal white line in (F), illustrating the occupancy (short arrow) or nonoccupancy (long arrow) of the center hole sites by C_{60} molecules.

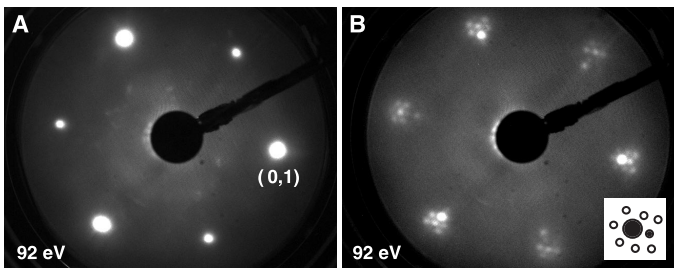

Fig. 2. LEED patterns from the clean Rh(111) surface (**A**) and from the surface covered with the *h*-BN nanomesh (40-L exposure) (**B**). One of the principal diffraction spots of the clean Rh(111) surface is labeled in (A). The inset in (B) illustrates the assignment of the adjacent group of spots: Rh(111) substrate spot (large filled circle), *h*-BN principal spot (small filled circle), and nanomesh superlattice spots (small open circles).

The double-layer character of the nanomesh is corroborated by ultraviolet photoelectron spectroscopy (UPS) data presented in Fig. 4. Upon exposure to 40 L of borazine and nanomesh formation, the normal emission spectrum shows an attenuation of the Rh signals and the appearance of two pairs of BN-related peaks. The binding energies of the individual pairs align well with the binding energies of the σ (5.3 eV) and the π (10.0 eV) states in normal emission spectra of *h*-BN MLs formed on Ni(111). The spectra thus expose the presence of two species of *h*-BN that have their binding energies for the σ and π band shifted by about 1 eV. From the intensity ratio of the two components of the σ band ($\sigma_1/\sigma_2 = 2.5 \pm 0.5$), we deduce the area ratio of the two species. Comparison with the model of Fig. 3A suggests that the lower binding energy component is associated with second-layer *h*-BN covering the first layer, whereas the higher binding energy component is from both the first and second layer where the *h*-BN is in direct contact with the metal substrate. For this assignment, an area ratio of roughly 3:1 should be expected. A similar band shift has been observed for the related graphite monolayer system on either clean (*14*) or *h*-BN–covered (*15*) Ni(111) surfaces.

On the basis of the analogy to the *h*-BN/Ni(111) system, we propose in Fig. 3, B and C, an atomic model for the nanomesh and how it registers with the Rh(111) substrate. The structure reflects the large lattice mismatch and the internal stiffness of the *h*-BN layer, and it maximizes the number of BN unit cells with adsorption sites close to the two types found on Ni(111). The stacking in the two-layer regions is that of solid *h*-BN where N and B are on top of each other and alternate layerwise. It is worth mentioning that this self-organization involves on the order of 400 atoms per mesh unit cell.

Higher tunneling currents can be used that bring the tip closer to the surface and access new electronic states. The edges of the top layer mesh are highlighted and thus appear to have a reduced tunneling resistance under these conditions (Fig. 1, D and E). A similar observation has been made along the edges of MoS_2 nanoclusters formed on Au(111) (*16*). Most likely, this effect is associated with edge states either because of unsaturated bonds or because of the presence of hydrogen. The image in Fig. 1E still permits us to guess the presence of the bottom layer. Likewise, the inset in Fig. 1A, showing a defect in the top layer, reveals the mesh structure of the bottom layer.

A further peculiarity in the STM imaging properties of the nanomesh is the small apparent step heights in the topographic image of Fig. 1B. The line profile in Fig. 1C indicates that the step height from the Rh surface layer to the first *h*-BN layer is only 0.5 Å. Likewise, the step height from first to second layer *h*-BN is only 0.5 Å. This value should be compared to the mean interlayer spacing of 1.92 Å determined by LEED (*10*) and x-ray photoelectron diffraction (*11*) for *h*-BN/Ni(111). A careful analysis of apparent film heights for this latter system found a pronounced dependence on the bias voltage, with a value of 1.1 Å at –2.0 V. It should be remembered that the *h*-BN films do not exhibit electronic states that contribute to the tunneling at these bias voltages. The STM images reflect the lateral changes of the tunneling resistance through the *h*-BN nanomesh (*9*). They may nevertheless be interpreted in a topographic way in the sense that step edges around the holes are clearly identified (*17*). More consistent step heights could be imaged in the following decoration experiment.

In order to illustrate the potential of the *h*-BN nanomesh for application as a template for the formation of supramolecular structures, we show in Fig. 1F a region of nanomesh after the room-temperature deposition of roughly a ML of C_{60} molecules. The periodicity of the mesh supercell is retained. The mesh wires are decorated by lines of individual molecules, whereas either six or seven molecules can be distinguished inside the holes. The corrugation of this molecular layer is now roughly 2 Å, which closely reflects the true depth of the second-layer nanomesh holes. The centers of the holes appear to be the least stable sites for molecular adsorption and may lend themselves to molecular manipulation. In the image of Fig. 1F, these sites are either empty or occupied by one C_{60} molecule,

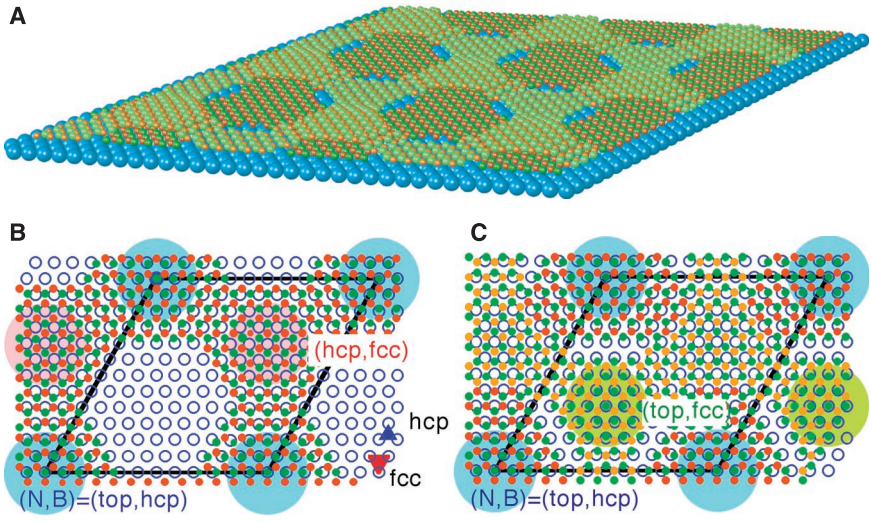

Fig. 3. Atomic model of the self-organized *h*-BN nanomesh based on the LEED and STM results. (**A**) Full three-dimensional model illustrating the two-layer character of the mesh and the corrugation of the upper layer. Rh (blue spheres), N (green spheres), and B (orange spheres) atoms are shown. The bottom *h*-BN layer is plotted in a darker hue. (**B**) Schematic drawing of the first layer of mesh, illustrating the proposed registry that may lead to the self-assembly. Rh atoms in the surface layer are represented as blue open circles, N atoms as dark green dots, and B atoms as red dots. The rhombus indicates the mesh unit cell. Regions with a predominant type of registry are color-shaded in blue or red, according to the corresponding adsorption sites (N,B) for N and B atoms relative to the top Rh layer. fcc, face-centered cubic; hcp, hexagonal close-packed. (**C**) Same as (B), but this time showing both the bottom and the top mesh layers. The light green circle shading indicates regions of predominantly top and fcc adsorption sites for N and B atoms, respectively.

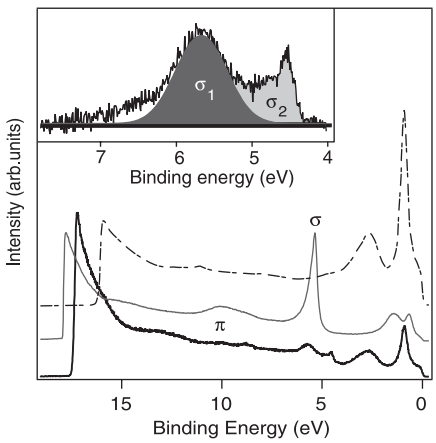

Fig. 4. Normal emission UPS ($h\nu = 21.2$ eV) spectra from the *h*-BN nanomesh on Rh(111) (thick solid line), from clean Rh(111) (dash-dotted line), and from one ML of *h*-BN on Ni(111) (thin solid line). arb., arbitrary. (**Inset**) The enlarged spectral region of the σ band and the decomposition into σ_1 and σ_2 contributions from *h*-BN that is in direct contact with the Rh(111) surface or separated by an additional *h*-BN layer.

which is seen more clearly in the line profile of Fig. 1G. At two places in the image, larger corralled protrusions appear at this center site, with an imaging height of 3 Å above the hole bottom. It is unclear whether they represent extra C_{60} on top of a first molecular layer or a first-layer molecule in a different state.

References and Notes

1. J. J. Pouch, S. A. Alterovitz, *Synthesis and Properties of Boron Nitride* (Trans Tech Publications, Enfield, NH, 1990).
2. F. Banhart, M. Zwanger, H.-J. Muhr, *Chem. Phys. Lett.* **231**, 98 (1994).
3. N. G. Chopra *et al.*, *Science* **269**, 966 (1995).
4. E. Bengu, L. D. Marks, *Phys. Rev. Lett.* **86**, 2385 (2001).
5. A. Nagashima, N. Tejima, Y. Gamou, T. Kawai, C. Oshima, *Phys. Rev. Lett.* **75**, 3918 (1995).
6. A. Nagashima *et al.*, *Phys. Rev. B* **51**, 4606 (1995).
7. W. Auwärter, T. J. Kreutz, T. Greber, J. Osterwalder, *Surf. Sci.* **429**, 229 (1999).
8. T. Greber *et al.*, *Surf. Rev. Lett.* **9**, 1243 (2002).
9. G. B. Grad, P. Blaha, K. Schwarz, W. Auwärter, T. Greber, *Phys. Rev. B* **68**, 085404 (2003).
10. Y. Gamou, M. Terai, A. Nagashima, C. Oshima, *Sci. Rep. Res. Inst. Tohoku Univ. Ser. A* **44**, 211 (1997).
11. M. Muntwiler *et al.*, *Surf. Sci.* **472**, 125 (2001).
12. W. Auwärter, M. Muntwiler, J. Osterwalder, T. Greber, *Surf. Sci.* **545**, L735 (2003).
13. M. Gsell, P. Jakob, D. Menzel, *Science* **280**, 717 (1998).
14. A. Nagashima, N. Tejima, C. Oshima, *Phys. Rev. B* **50**, 17487 (1994).
15. A. Nagashima, Y. Gamou, M. Terai, M. Wakabayashi, C. Oshima, *Phys. Rev. B* **54**, 13491 (1996).
16. S. Helveg *et al.*, *Phys. Rev. Lett.* **84**, 951 (2000).
17. The low corrugation observed in the constant-current STM images of the nanomesh provides a strong argument against the incorporation of Rh atoms into the mesh structure and substrate etching below the nanomesh.

18. We thank H. Sachdev for providing us the borazine, E. Stoll for generating the three-dimensional figure of the nanomesh, and M. Klöckner for technical assistance. Supported by the Swiss National Science Foundation.

Supporting Online Material

www.sciencemag.org/cgi/content/full/303/5655/217/DC1

Fig. S1

29 September 2003; accepted 2 December 2003

Periodic Pulsing of Characteristic Microearthquakes on the San Andreas Fault

Robert M. Nadeau* and Thomas V. McEvilly

Deep fault slip information from characteristically repeating microearthquakes reveals previously unrecognized patterns of extensive, large-amplitude, long-duration, quasiperiodic repetition of aseismic events along much of a 175-kilometer segment of the central San Andreas fault. Pulsing occurs both in conjunction with and independent of transient slip from larger earthquakes. It extends to depths of ~10 to 11 kilometers but may be deeper, and it may be related to similar phenomena occurring in subduction zones. Over much of the study area, pulse onset periods also show a higher probability of larger earthquakes, which may provide useful information for earthquake forecasting.

Aseismic fault slip along the transform plate–bounding San Andreas fault (SAF) in central California is commonly assumed to occur at a relatively constant rate modulated by localized slip transients induced by moderate and large earthquakes (*1*). Studies of large-scale, time-dependent deep fault slip along this stretch of fault have been limited, however, by the distribution and frequency of deformation measurements and by the fundamental trade-offs and assumptions required to infer deep slip from measurements of surface motion (*2*–*9*). We studied time-dependent deep fault slip within the seismogenic zone (i.e., the brittle upper crust where earthquakes occur) along 175 km of the central creeping section of the SAF (Fig. 1) over a 16-year period beginning in 1984, using the seismic moments and recurrence intervals from 2594 characteristically repeating microearthquakes.

Characteristic microearthquakes have special properties (*10*), allowing a relation between their seismic moments (M_0) and the surrounding aseismic fault slip (d_i) that loads their rupture patches to failure during the recurrence interval preceding each event (*10*).

$$d_i = 10^{\alpha} M_0^{\beta} \quad (1)$$

Once parameters α and β are determined (*10*), Eq. 1 can then be used to infer the history of deep slip rates on fault segments that contain characteristic microearthquakes (*10*) (fig. S2).

A profile of long-term deep slip rates for the 175-km study zone was derived from the characteristic microearthquake data (*10*), and the distribution of these rates is generally consistent with long-term geodetic rates in the study zone (*1*, *2*, *5*–*7*) (Fig. 2A). A profile of short-term slip-rate histories for the study zone was also constructed (*10*) (Fig. 2B). Common short-term features between the microearthquake slip and geodetic rates (*5*) are also apparent; however, their general consistency is lower than it is for the long-term rates. For example, the patterns of strong, quasiperiodically recurring slip-rate pulses seen in the microearthquake slip data are only vaguely apparent in the fault-creep data (*10*) (Fig. 2C). Characteristic microearthquake slip and seismicity rates (*10*) along the study zone also correlate somewhat (Fig. 2C), although differences associated with aftershocks and earthquake swarms are often observed.

Six regions with distinct patterns of complexity and slip-rate evolution can be identified in the study zone (Figs. 1 and 2). In regions IV and V, fault structure is relatively simple and few large earthquakes [magnitude (M) > 3.5] occurred during the study period. Slip-rate histories in these regions are dominated by previously unrecognized quasiperiodic pulses having relatively constant peak amplitudes, rate variations of 100% or more, and cycle durations of about 3.0 and 1.7 years, respectively (Fig. 2C, segments c and d). These pulsing patterns are not directly associated with the occurrence of any nearby large earthquakes. Analyses of the data using subsets in depth show that the pulsing patterns are similar throughout the depth range of the data, and this is a common feature of the slip patterns throughout the study zone.

The relatively abrupt transition between the pulsing patterns in regions IV and V is not associated with any obvious seismogenic zone complexities, and the pulsing between these regions is not correlated (fig. S4). This suggests that their pulsing is not driven by coherent large-scale phenomena such as gravitational tides or pulsed loading by the adjacent tectonic plates. It also suggests that the mechanisms responsible for their pulsing are relatively independent of one another. The confinement of these mechanisms to the approximate fault zone can also be inferred because broadly distributed mechanisms would probably result in more diffuse transition zones between adjacent pulsing regions.

In region VI, the SAF changes from freely creeping to fully locked behavior and spans a locked patch of fault that has ruptured repeatedly in several M6 earthquakes at Parkfield (*11*). Variations in the short-term deep slip-rate histories for this region

Berkeley Seismological Laboratory, 211 McCone Hall, University of California, Berkeley, CA 94720–4760, USA.

*To whom correspondence should be addressed. E-mail: nadeau@seismo.berkeley.edu